ELSEVIER

Journal of Power Sources 77 (1999) 127–135

JOURNAL OF POWER SOURCES

The effect of cathode porosity on the performance of a cylindrical alkaline cell

J.J. Kriegsmann, H.Y. Cheh *

Department of Chemical Engineering and Applied Chemistry Columbia University, 812 S.W. Mudd, Mailcode 4721, 500 West 120th Street, New York, NY 10027, USA

Received 28 October 1998; accepted 6 November 1998

Abstract

The effects of varying initial cathode porosity on the discharge performance of an AA-size Zn/MnO_2 alkaline cell are studied. An existing model is used to simulate cell behavior. Cell discharge time is chosen as the quantity to maximize for a continuous galvanostatic discharge with a prescribed cutoff voltage. An algorithm is developed that compensates for changes in initial cathode porosity by altering initial anode porosity, with initial separator porosity maintained constant. A constant capacity ratio and fixed external cell geometry are also constraints in this procedure. A different approach is incorporated into the design scheme whereby cathode void volume is obtained by removing graphite from the cathode solid material, without accounting for expected matrix conductivity changes. For each amount of graphite removed, the model predicts an optimum initial porosity for maximizing the discharge time. The longest discharge time occurs when all graphite is removed from the cathode. The influence of effective cathode matrix conductivity is investigated separately. © 1999 Elsevier Science S.A. All rights reserved.

Keywords: Alkaline batteries; Porosity; Discharge time; Conductivity; Graphite

1. Introduction

Podlaha and Cheh [1,2] have presented a model for primary cylindrical AA-size alkaline cells under high discharge rate conditions. Simulations have been conducted for galvanostatic, constant load, and constant power modes for either continuous or pulse discharges. A goal of the Zn/MnO_2 alkaline cell modeling is to ascertain operating conditions that enhance cell performance for the broadest number of applications. The model predicts actual discharges with reasonable accuracy. Optimization of cell behavior is now sought for this system in conjunction with the mathematical model.

Two simulation approaches appear in the literature. The first involves the use of a sensitivity coefficient, usually chosen to reflect cell voltage changes in response to perturbations in a parameter of interest [3–5]. As stated by Evans and White [3], the main value of the coefficient is its utility in prioritizing any research effort involving parameter estimation. If a model is highly responsive to a certain parameter, then more resources should be devoted toward achieving its most accurate value. The second method attempts to improve cell behavior by identifying a best design [6–10]. This is achieved through variations in cell geometry and solid material loading, and can be divided into two groups: investigations using fully developed computational models [6–9], and those with simplified analytical models [10].

At high rates of discharge, ionic transport limits the Zn/MnO_2 cylindrical alkaline cell performance. The cathode region in this system has much less porosity than the anode and separator regions. It is assumed that an increase in initial cathode porosity would reduce transport limitations throughout the cathode and benefit overall cell performance. Because of external geometry and active material requirements, initial cathode porosity cannot vary independently of many other cell parameters. Therefore, a sensitivity coefficient analysis is not applicable as an optimization procedure.

According to Newman [10], the total cell discharge time ‘‘can be regarded as the most important parameter of the intended application that governs the design of an actual

* Corresponding author. Tel.: +1-212-854-4453; Fax: +1-212-854-3054; E-mail: hyc1@columbia.edu

0378-7753/99/$19.00 © 1999 Elsevier Science S.A. All rights reserved.
PII: S0378-7753(98)00185-2

system.'' Although Newman maximized the specific energy using a Ragone plot, it is apparent in the current work involving the Zn/MnO_2 cell that the maximization of discharge time itself is a simple and meaningful approach consistent with enhancing overall cell performance. This quantity can then be related to other variables in future work. Therefore, an investigation is performed that attempts to maximize the Zn/MnO_2 cell discharge time for a commercially relevant discharge scheme, through variations in the initial cathode porosity.

2. Porosity terms in the theoretical model

Podlaha and Cheh's model [1,2] is now discussed in the context of electrode porosity effect on discharge performance. The schematic of a cylindrical Zn/MnO_2 alkaline cell is shown in Fig. 1. As the model is one-dimensional, only the radial coordinate is considered. All three cell regions are porous. Initially, the cathode contains electrolytic manganese dioxide (EMD) with a graphite filler, the anode is composed of porous zinc, and the separator matrix is a nonreacting solid component. The electrolyte contains KOH and potassium zincate, $K_2Zn(OH)_4$, at high concentrations. The four radii listed are r_{ac}, the anode current collector/anode interface location, r_a, the anode/separator interface location, r_s, the separator/cathode interface location, and r_c, the cathode/cathode current collector interface location. The cell height is given by L.

Throughout a discharge, the following reactions are modeled. In the anode, zinc oxidizes to form zincate ion:

$$Zn + 4OH^- \rightarrow Zn(OH)_4^{2-} + 2e^-. \quad (1)$$

The zincate ion then precipitates to form solid zinc oxide:

$$Zn(OH)_4^{2-} \rightarrow ZnO + H_2O + 2OH^-. \quad (2)$$

In the cathode, EMD is reduced to form groutite, also known as manganese oxyhydroxide [11]:

$$MnO_2 + H_2O + e^- \rightarrow MnOOH + OH^-. \quad (3)$$

The model considers only a one-electron discharge in the cathode.

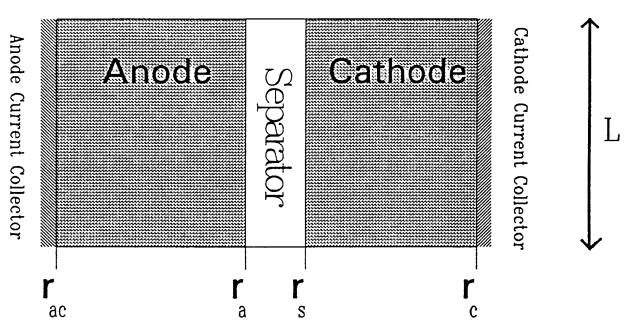

Fig. 1. Cell schematic for a cylindrical Zn/MnO_2 alkaline cell.

Porosity appears in the electrolyte material balance equations for species i [12,13]:

$$\frac{\partial \epsilon c_i}{\partial t} = -\nabla \cdot \boldsymbol{N}_i + R_i \quad (4)$$

where ϵ is porosity, c_i is the concentration of ionic species i, N_i is the molar flux of species i, and R_i is a generalized source term per unit volume for species i that accounts for electrochemical reaction and chemical precipitation. This equation is applied to hydroxyl and zincate ions. Porosity is also seen in expressions for effective transport properties, as in Ohm's law in the electrolyte phase, and molar fluxes for hydroxyl and zincate ions.

For the $KOH/K_2Zn(OH)_4/H_2O$ ternary electrolyte system, Ohm's law in the electrolyte phase has the following general form [13–15]:

$$\nabla\eta = \boldsymbol{i}_2\left(\frac{1}{\kappa\epsilon^{1.5}} + \frac{1}{\sigma}\right) - \frac{\boldsymbol{I}}{\sigma} + \frac{1}{nF}\left(\frac{s_1}{\nu_{1A}} + \frac{nt_1}{z_1\nu_{1A}} - \frac{s_0}{c_0}c_1\right)\nabla\mu_A + \frac{1}{nF}\left(\frac{s_2}{\nu_{2B}} + \frac{nt_2}{z_2\nu_{2B}} - \frac{s_0}{c_0}c_2\right)\nabla\mu_B \quad (5)$$

where κ and σ are the electrolyte and effective matrix conductivities, respectively, η is the local overpotential, c_1 is the zincate ion concentration, c_2 is the hydroxyl ion concentration, c_0 is the solvent concentration, s_i is the stoichiometric coefficient for species i in the arbitrary reference electrode reaction, ν_{1A} and ν_{2B} are the number of molecules of species i ($1 = Zn(OH)_4^{2-}$, $2 = OH^-$) that can dissociate completely from one molecule of salt A or B ($A = K_2Zn(OH)_4$, $B = KOH$), and z_i is the charge number for ionic species i. The respective electrochemical potentials for the potassium zincate and potassium hydroxide aqueous salts are given by μ_A and μ_B, $\boldsymbol{i}_2$ is the superficial current density in the electrolyte phase, and $\boldsymbol{I}$ is the total cell current density. Ohm's law in the electrolyte phase is applied in each cell region. This is the only governing equation where σ and κ appear. The effective matrix conductivities are given by σ_a and σ_c for the anode and cathode regions, respectively. This form of Ohm's law in the electrolyte phase has no specified reference electrode, and additional terms that describe solid solution theory are necessary for this equation to be valid in the cathode region.

The term $\kappa\epsilon^{1.5}$ is the effective electrolyte conductivity accounting for the porous nature of the cell. This notation differs from that chosen for σ, which itself is an effective conductivity with its dependence on porosity internalized. For the anode [1,14]:

$$\sigma_a = \sum_i \sigma_i \epsilon_i^{1.5}, \quad (6)$$

where the summation is over all solid species present in the anode, ϵ_i is the solid volume fraction of species i, and σ_i is the electrical conductivity of solid species i, which includes zinc, zinc oxide, and mercury. The cathode effective matrix conductivity is constant, and the separator effective matrix conductivity is assumed negligible [15].

The molar flux equations for the zincate and hydroxyl ions are given by [13–15]:

$$\boldsymbol{N}_1 = -D_A \epsilon^{1.5} \nabla c_1 + \frac{t_1}{z_1 F} \boldsymbol{i}_2 + c_1 \boldsymbol{v} \tag{7}$$

$$\boldsymbol{N}_2 = -D_B \epsilon^{1.5} \nabla c_2 + \frac{t_2}{z_2 F} \boldsymbol{i}_2 + c_2 \boldsymbol{v}. \tag{8}$$

Here, D_A and D_B are the respective salt diffusion coefficients for $K_2Zn(OH)_4$ and KOH, t_1 and t_2 are transference numbers with respect to the volume average velocity for the zincate and hydroxyl ions, respectively, and $\boldsymbol{v}$ is the volume average velocity of the electrolyte. Effective diffusivities are given by $D_A \epsilon^{1.5}$ and $D_B \epsilon^{1.5}$. Porosity and volume average velocity are coupled, as shown in Ref. [1]. Porosity can change in a region due to the difference of molar volumes of solid products and reactants, as well as by chemical precipitation of solid zinc oxide. Changes in porosity can then create electrolyte convection within the cell.

It is expected that the greatest effect of porosity on cell performance is due to its influence on the effective electrolyte conductivity and the effective salt diffusivities. Increasing the cathode porosity increases these quantities in the cathode region. This will result in reduced local gradients of overpotential and electrolyte concentrations for a particular cell current value, which should lower the polarization loss in the cathode. The cell voltage calculation is quite sensitive to local overpotential, which is described by Eq. (5) and is present in the electrochemical reaction rate terms, of mainly Butler–Volmer form, shown in Ref. [1]. Cell voltage as a function of time is given by:

$$E = E_0 + \frac{2RT}{F} \ln\left(\frac{1-f}{f}\right) + \eta(r_a^+) - (\eta(r_a) + \eta(r_{ac})) \tag{9}$$

where f is depth of discharge of the cell assuming a cathodically limited system based on a one-electron discharge reaction of MnO_2, and E_0 is taken as 1.34 V at the reference state of $f = 0.5$ [1]. The first two terms on the right hand side are the open circuit potential terms collectively referred to as the Tye equation [16]. Actual changes in porosity throughout a discharge are not expected to be as significant as absolute porosity values. This point can be appreciated from the observation that many researchers neglect convection effects and porosity changes in their models [4–10].

3. Optimization strategy

The objective is to find the initial cathode porosity that gives the best cell performance according to Podlaha and Cheh's [1,2] model for an AA-size Zn/MnO_2 alkaline cell. The relevant input parameters for this system are given in Table 1 [1]. The selected mode of operation is a continuous 1.0 A galvanostatic discharge with a 0.8 V cutoff voltage, which is an industrially useful high-rate test condition [17].

To be considered commercially viable, any initial cathode porosity change must not alter the external geometry. Therefore, any increase in initial cathode porosity from a reference condition must decrease the void volume of either the anode region, the separator region, or both regions simultaneously. When the active material is not removed from either electrode, and separator volume and initial separator porosity remain unchanged, the problem reduces to compensating anode void volume in favor of additional cathode void volume. This requires changing the following Table 1 quantities: r_s, r_a, ϵ_c^0, the initial cathode porosity, ϵ_a^0, the initial anode porosity, and ϵ_{Zn}^0, the initial zinc active material volume fraction. Because the above procedure varies r_a and r_s, it is referred to as the 'variable electrode length' design scheme, whereby electrode porosity and electrode length are directly related.

Additional cathode porosity can also be obtained by removing graphite filler from the cathode solid matrix. Graphite is added as a conducting agent and can range from 8–12 wt.% of total solid material in the cathode [15]. By itself this would not require any variation of internal radii. In this investigation, graphite removal is combined with the variable electrode length scheme. Graphite re-

Table 1
Base case system quantities [1]

L	4.15 cm
r_{ac}	0.09 cm
r_a	0.43 cm
r_s	0.45 cm
r_c	0.66 cm
c_2^0	0.007 mol/cm^3
c_1^0	5.3×10^{-4} mol/cm^3
w_{act}	8.39 g
Anode active material	3.71 g
ϵ_a^0	0.74
ϵ_{Zn}^0	0.251
ϵ_{ZnO}^0	0
ϵ_{Hg}^0	0.009
ϵ_s^0	0.8
ϵ_c^0	0.24
σ_c	19.8 Ω^{-1} cm^{-1}
T^0	298.15 K
i_0 cathode	2.0×10^{-7} A/cm^2
α_a cathode	0.5
α_c cathode	0.5
a_c^0	1200 cm^{-1}
Q	0.308 Ah/g-MnO_2
f^0	0.00631

moval would lower the cathode effective matrix conductivity, σ_c, but in the following analysis σ_c is left at its base case value. The optimization with respect to initial cathode porosity is performed with the assumed value of 10 wt.% graphite, or $\omega_G = 0.10$.

4. Variable electrode length algorithm

The equations needed to determine the input values of r_s, r_a, ϵ_a^0, and ϵ_{Zn}^0 for a selected value of ϵ_c^0 are now presented. The first step is to choose a value for ϵ_c^0, the initial cathode porosity. Let $V_{EMD/G}^0$ denote the total solid volume in the cathode with no graphite removed. This quantity is determined from base case values. For the general case of graphite removal, $V_{EMD/G}^0$ is altered to give $V_{EMD/G}$, the total solid volume in the cathode from:

$$V_{EMD/G} = V_{EMD/G}^0 - \chi V_G \tag{10}$$

where χ is the fractional value of graphite removed, and V_G is the volume of graphite present for the base case. The total graphite volume available for removal is determined from:

$$V_G = \frac{w_G}{\rho_G} \tag{11}$$

where w_G is the weight of graphite filler, and ρ_G is the graphite density. The cathode volume is then calculated from:

$$V_{cath} = \frac{V_{EMD/G}}{1 - \epsilon_c^0} \tag{12}$$

With the new cathode volume, r_s is solved by rearrangement of the equation describing the annular volume of the cathode region:

$$r_s = \left(r_c^2 - \frac{V_{cath}}{\pi L} \right)^{1/2}. \tag{13}$$

The fixed values for r_c and L are given in Table 1. The separator volume is given by:

$$V_{sep} = \pi\left(r_s^2 - r_a^2 \right) L. \tag{14}$$

Table 2
Additional base case system quantities

ρ_G	2.26 g/cm^3 [18]
$V_{EMD/G}^0$	2.33 cm^3
V_G	0.41 cm^3
ω_G	0.10
w_G	0.93 g
V_{sep}	0.23 cm^3
$V_{Zn/Hg}$	0.61 cm^3

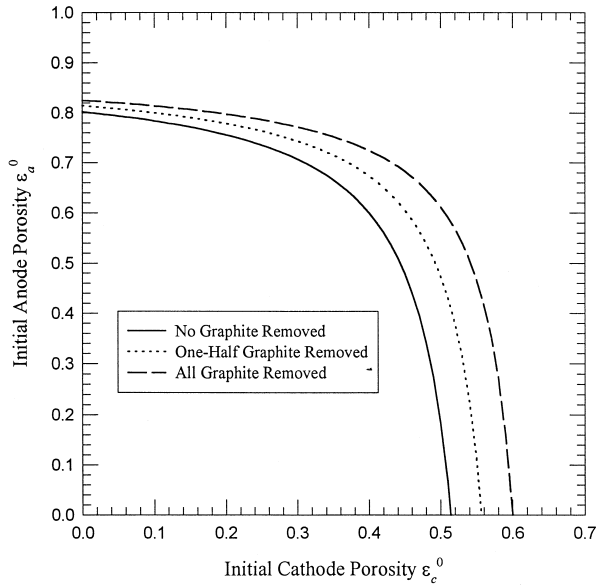

Fig. 2. Initial anode porosity vs. initial cathode porosity for the variable electrode length design scheme.

Although V_{sep} is constant, r_a must be calculated because r_s is altered using Eq. (13), whereby:

$$r_a = \left(r_s^2 - \frac{V_{sep}}{\pi L} \right)^{1/2}. \tag{15}$$

The anode volume, V_a, is computed from:

$$V_a = \pi\left(r_a^2 - r_{ac}^2 \right) L \tag{16}$$

where r_{ac} is fixed at its value in Table 1.

Only zinc and mercury are initially present as solid materials in the anode. The volume displaced by these components at the beginning of discharge, $V_{Zn/Hg}$, is a fixed value for the variable electrode length scheme and is calculated from base case numbers. The initial volume fraction of zinc and mercury is found from:

$$\epsilon_{Zn/Hg}^0 = \frac{V_{Zn/Hg}}{V_a} \tag{17}$$

where $\epsilon_{Zn/Hg}^0$ is defined as

$$\epsilon_{Zn/Hg}^0 = \epsilon_{Zn}^0 + \epsilon_{Hg}^0 \tag{18}$$

with ϵ_{Hg}^0, the initial mercury volume fraction in the anode, constant throughout the algorithm. Because the initial solid volume fractions in the anode and the initial anode porosity sum to unity, the initial anode porosity is given by:

$$\epsilon_a^0 = 1 - \epsilon_{Zn}^0 - \epsilon_{Hg}^0 \tag{19}$$

Additional quantities necessary for the input parameter algorithm are listed in Table 2. The calculations of V_{cath}, r_s, r_a, V_a, ϵ_{Zn}^0, and ϵ_a^0, for a range of ϵ_c^0 values parametrized by the fraction of graphite removed, represent the solved input parameter conditions for this optimization scheme. Fig. 2 shows initial anode porosity as a function of initial cathode porosity. The higher the graphite

content at a certain initial cathode porosity value, the smaller is the initial anode porosity. Only positive values of ϵ_a^0 are possible, and for each amount of graphite removed there is a maximum allowable value of ϵ_c^0. Similar curves for V_{cath}, r_s, r_a, V_a, and ϵ_{Zn}^0 can be constructed.

The algorithm is now included in the numerical solution of the coupled, nonlinear partial differential equations describing the battery system in the radial and time coordinates [1,2]. A pentadiagonal BAND(J) solver [19,20] is used with a modified numerical linearization subroutine [15,21] and the Crank–Nicolson method. The runs span from minimum to maximum ϵ_c^0 values for three cases: no graphite removed, one-half graphite removed, and all graphite removed.

5. Results

5.1. Effect of graphite removal using the base case internal geometry

Before analyzing the main results of varied initial cathode porosity combined with internal radii changes, the effect of graphite removal on discharge time is assessed for the base case geometry with ϵ_c^0 changing only as a result of graphite removal. Table 3 lists results for three cases: no graphite removed, one-half graphite removed, and all graphite removed. Total depth of discharge values are also given. For a galvanostatic discharge, depth of discharge at the cell cutoff voltage, f_d, is calculated from Ref. [1]:

$$f_d = \frac{It_d}{Qw_{act}} + f^0 \tag{20}$$

where Q is the theoretical capacity of the cathode active material, w_{act} is the cathode active material amount, I is the cell current, t_d is the discharge time to reach the cutoff voltage, and f^0 is a numerical factor to ensure an open circuit potential of 1.6 V at the beginning of discharge [22]. The increase in discharge time is substantial for each degree of graphite removal. Thus, graphite removal for a particular internal cell geometry is beneficial. Fig. 3 displays performance curves that describe the results of Table 3. At early stages of discharge there is not much difference between the three cases, but when cell voltage drops below 1.0 V the trends become distinct. When all graphite is removed, the curve is superior to the others.

Table 3
Graphite removal effect for the base case geometry

Scheme	ϵ_c^0	ϵ_a^0	r_a (cm)	r_s (cm)	t_d (h)	f_d
No graphite removed	0.24	0.74	0.43	0.45	0.700	0.277
One-half graphite removed	0.307	0.74	0.43	0.45	0.861	0.339
All graphite removed	0.374	0.74	0.43	0.45	0.939	0.370

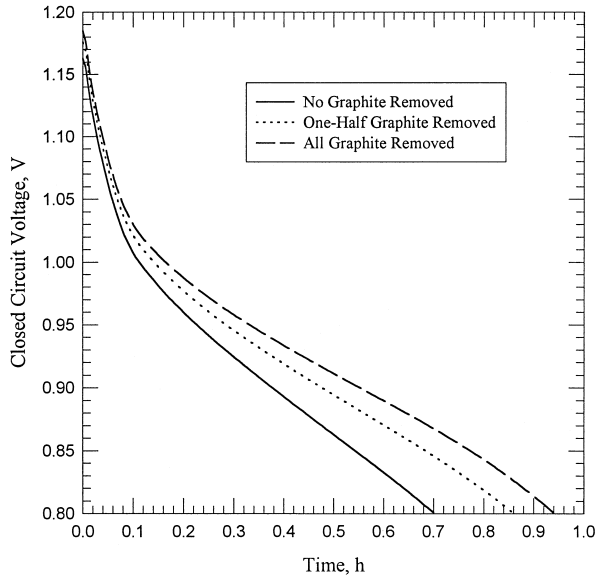

Fig. 3. Cell voltage curves for the base case geometry with cathode graphite removal.

5.2. Variable electrode length optimization results

Fig. 4 presents discharge time as a function of initial cathode porosity for the three conditions of graphite removal with variable internal radii. It is similar to figures shown by Evans et al. [23]. Continuing with the trend observed in Table 3, Fig. 4 shows that graphite removal causes dramatic improvements in discharge time, before reaching the cutoff voltage, when variable electrode lengths

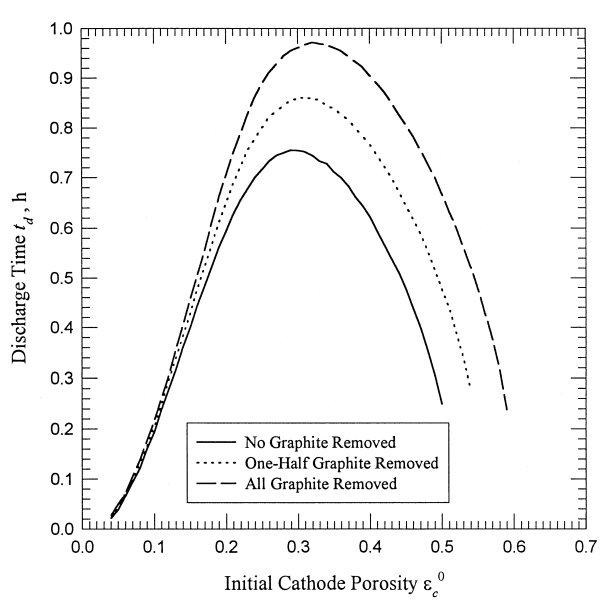

Fig. 4. Variable electrode length design scheme results.

are permitted. The most interesting fact about Fig. 4 is the occurrence of well-defined maximum discharge times at certain initial cathode porosity values, for each degree of graphite removal. This reflects the balancing of competing effects occurring throughout the cell as predicted by the model. Identifying these effects is complicated by the highly coupled form of the battery governing equations. The inherently low initial cathode porosity leads to the choice of cathode effective electrolyte conductivity as a very important quantity, even though the region is under activation control for low discharge rates [24]. The anode is more difficult to analyze because of the complex behavior in this region. However, at small initial anode porosities the ohmic effect due to a lessened effective electrolyte conductivity may also become vital. Because the current distribution is more nonuniform in the anode than in the cathode, the coupling of effective electrolyte conductivity to local overpotential may introduce more severe effects in terms of modeled cell performance.

Table 4 summarizes the results of Fig. 4 by listing the best cases for the three graphite removal scenarios. When no graphite is removed, the maximum discharge time occurs with $\epsilon_c^0 = 0.290$, with a discharge time improvement of 0.055 h, or 7.9%, compared to the base case with no graphite removed.

When one-half graphite content is removed, the best case is observed for $\epsilon_c^0 = 0.310$, and the predicted discharge time is 0.861 h. This discharge time is identical to that shown in Table 3, with one-half graphite removed but with the base case geometry. Here, the variable electrode length technique does not offer improvement over the base case geometry. However, the t_d value of 0.861 h for one-half graphite removed, with variable internal radii, is a 0.161 h or 23% simulated increase in cell life before the cutoff voltage, compared to the base case with no graphite removed.

The greatest predicted improvement in cell life before reaching the cutoff voltage is achieved when all graphite is removed, with $\epsilon_c^0 = 0.320$. The maximum simulated discharge time is 0.972 h, as shown in Table 4. This value, which corresponds to all graphite removed and variable internal radii, is the longest discharge time calculated by the optimization scheme. When the Table 4 value for all graphite removed is compared to the base case with no graphite removed in Table 3, the increase in discharge time is 0.272 h, or 39%. Fig. 5 presents cell voltage curves for the best cases listed in Table 4. As with Fig. 3, the cell voltage curves are noticeably different below 1.0 V.

Table 4
Best case results of the variable electrode length simulations

Scheme	ϵ_c^0	ϵ_a^0	r_a (cm)	r_s (cm)	t_d (h)	f_d
No graphite removed	0.290	0.714	0.414	0.435	0.755	0.298
One-half graphite removed	0.310	0.739	0.432	0.452	0.861	0.339
All graphite removed	0.320	0.765	0.455	0.474	0.972	0.382

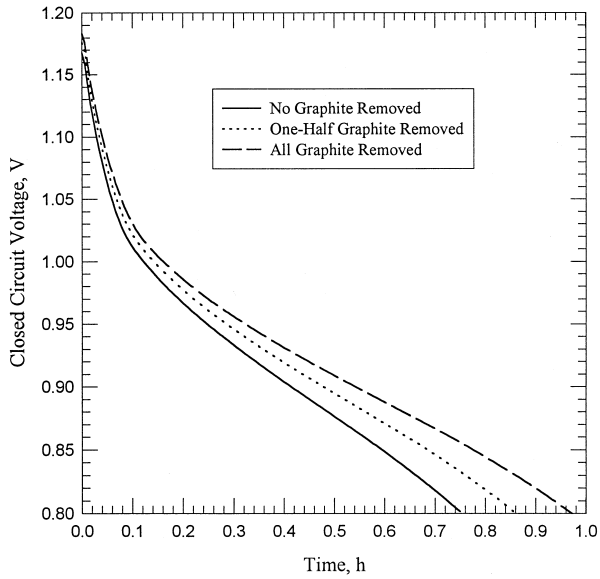

Fig. 5. Cell voltage curves for the best case results from the variable electrode length design scheme.

6. Cathode effective matrix conductivity

The best case simulation result with all graphite removed is an idealization because cathode effective matrix conductivity, σ_c, must decrease with graphite removal. There are two main reasons why the dependence of σ_c on graphite weight fraction is ignored in this investigation. The first consideration involves the benefits of using a first-order approach. Polarization effects are then directly attributable to initial cathode porosity and internal geometry changes due to this initial condition. Uncertainty in quantifying which parameter, ϵ_c^0 or σ_c, is more influential with respect to cell performance is thus avoided. Secondly, there is an insufficiency of data regarding the variation of conductivity on the amount of graphite. Podlaha and Cheh [1] did not list the source for their σ_c value. However, the literature gives only ranges of EMD conductivity values that vary by several orders of magnitude [1,25–28]. Such wide variation in EMD electrical conductivities would require a more extensive investigation prior to including conductivity functions involving a graphite weight fraction dependency.

Valuable information can be obtained by examining how the model responds to changes in cathode effective matrix conductivity directly. For this aspect of the investi-

gation, only the base case geometry described by Table 1 is used. In addition to parameters listed by Newman and Tiedemann [12], Chen and Cheh [24] also identified a curvature parameter as being important in governing the current distribution of a cylindrical porous electrode. However, with cathode effective matrix conductivity as the only parameter being varied, this shape parameter does not need to be considered. Also, since only σ_c is changed, three of the four parameters listed in Ref. [12] are required in the current distribution study.

The relevant parameters that depend on σ_c are a dimensionless cell current:

$$\delta = \frac{\alpha_a F I(r_c - r_s)}{RT^0 2\pi \frac{(r_s + r_c)}{2} L}\left(\frac{1}{\kappa^0(\epsilon_c^0)^{1.5}} + \frac{1}{\sigma_c}\right), \tag{21}$$

a dimensionless exchange current density:

$$\nu^2 = \frac{(\alpha_a + \alpha_c) F a_c^0 i_0 (r_c - r_s)^2}{RT^0}\left(\frac{1}{\kappa^0(\epsilon_c^0)^{1.5}} + \frac{1}{\sigma_c}\right), \tag{22}$$

and the ratio of matrix to electrolyte effective conductivities:

$$\gamma = \frac{\sigma_c}{\kappa^0(\epsilon_c^0)^{1.5}}. \tag{23}$$

In the above three equations, κ^0 is a characteristic value of the electrolyte conductivity, T^0 is the initial cell temperature, α_a and α_c are the respective anodic and cathodic transfer coefficients for the cathode electrochemical reaction, a_c^0 is the initial specific interfacial area in the cathode, and i_0 is the cathode exchange current density evaluated at a reference condition. These quantities are listed in Table 1. The κ^0 $(\epsilon_c^0)^{1.5}$ term denotes effective initial electrolyte conductivity in the cathode.

As stated by Doyle et al. [29], when either δ or ν^2 is much larger than unity the reaction distribution is nonuniform because the system is ohmically limited. A large value of γ shifts the reaction to the separator/cathode interface. Cathode effective matrix conductivity is varied from its base case value by several orders of magnitude, both above and below its Table 1 value. For each new value of σ_c, a 1.0 A continuous discharge with a cutoff voltage of 0.8 V is performed for the base case geometry. Table 5 lists values given by Eqs. (21)–(23) as well as the discharge time for each run.

Surprisingly, as matrix conductivity is decreased, discharge time increases. Since the runs are performed at a high discharge rate, δ may be more important than ν^2. For the base case δ is about 4.00. However, this value may not be construed as much larger than unity and the system can be considered under activation control. Above $\sigma_c = 19.8$

Table 5
Discharge times and current distribution parameters for various cathode effective matrix conductivities using the base case geometry

σ_c (Ω^{-1} cm^{-1})	δ	ν^2	$\sigma_c/\kappa^0(\epsilon_c^0)^{1.5}$	t_d (h)
19.8×10^{-4}	145.9	2.160×10^{-1}	2.807×10^{-2}	1.211
19.8×10^{-3}	18.17	2.691×10^{-2}	2.807×10^{-1}	0.961
19.8×10^{-2}	5.402	7.999×10^{-3}	2.807	0.739
19.8×10^{-1}	4.125	6.108×10^{-3}	28.07	0.706
19.8	3.997	5.919×10^{-3}	2.807×10^{2}	0.700
198	3.984	5.900×10^{-3}	2.807×10^{3}	0.700
19.8×10^{2}	3.983	5.898×10^{-3}	2.807×10^{4}	0.700
19.8×10^{3}	3.983	5.898×10^{-3}	2.807×10^{5}	0.700

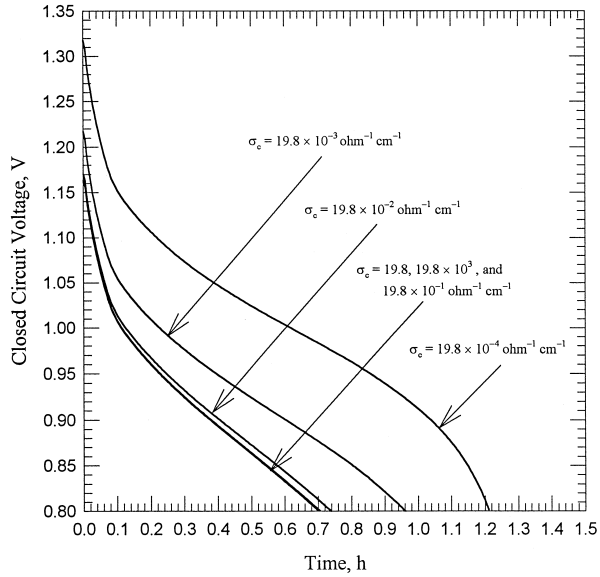

Fig. 6. Cell voltage curves for the base case geometry with the cathode effective matrix conductivity varied.

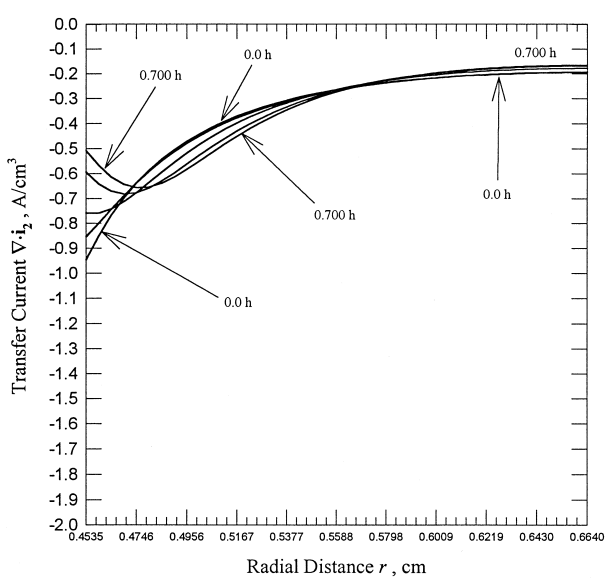

Fig. 7. Transfer current profiles throughout the cathode for the base case geometry with $\sigma_c = 19.8\ \Omega^{-1}\ \text{cm}^{-1}$.

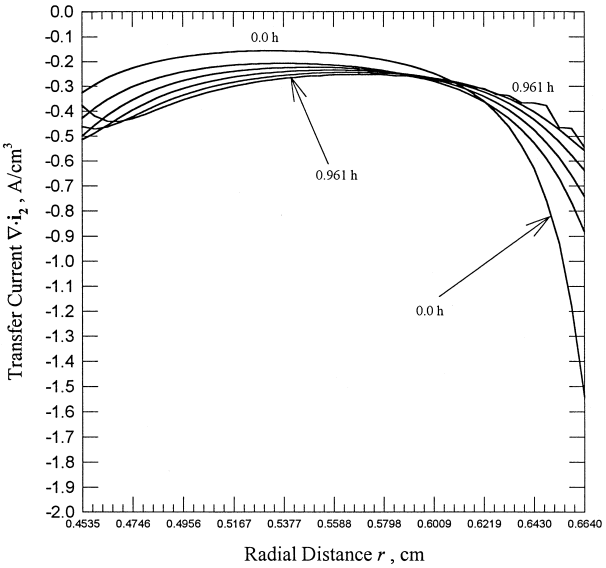

Fig. 8. Transfer current profiles throughout the cathode for the base case geometry with $\sigma_c = 19.8 \times 10^{-3}\ \Omega^{-1}\ \mathrm{cm}^{-1}$.

$\Omega^{-1}\ \mathrm{cm}^{-1}$, δ and ν^2 remain virtually unchanged, and the discharge times are identical; γ is much larger than unity. Below the base case effective matrix conductivity value, δ increases substantially while γ decreases. Therefore, when σ_c is increased, the current distribution is not expected to change much from the base case simulation. When σ_c is decreased, the reaction profile should become nonuniform, but a very low γ value should shift the current distribution to within the cathode. Fig. 6 shows voltage profiles outlined by Table 5. Performance is indistinguishable when σ_c is above 19.8 $\Omega^{-1}\ \mathrm{cm}^{-1}$. The curve with the maximum discharge time is characterized by $\sigma_c = 19.8 \times 10^{-4}\ \Omega^{-1}\ \mathrm{cm}^{-1}$. Fig. 6 is analogous to one shown by Doyle et al. [7].

The two simulations corresponding to $\sigma_c = 19.8\ \Omega^{-1}\ \mathrm{cm}^{-1}$ and $\sigma_c = 19.8 \times 10^{-3}\ \Omega^{-1}\ \mathrm{cm}^{-1}$ are now analyzed in terms of their current distributions. Fig. 7 presents transfer current in the cathode with the base case σ_c value. The current distribution is nonuniform with a large reaction rate at the separator/cathode interface. Throughout the discharge, there is a slight front-like trend in transfer current close to the separator interface. The region near the cathode current collector maintains relatively low transfer current throughout the discharge.

Fig. 8 is the transfer current distribution in the cathode with $\sigma_c = 19.8 \times 10^{-3}\ \Omega^{-1}\ \mathrm{cm}^{-1}$. This figure is quite different from Fig. 7. The reaction is not skewed towards the separator/cathode interface, but there is a very large initial reaction rate at the cathode current collector. As discharge time progresses the reaction distribution becomes more uniform throughout the cathode. Discharge time is increased because the total cathodic overpotential is decreased with respect to the base case. This must result from the more uniform consumption of MnO_2 active material. Figs. 7 and 8 support the results shown in Table 5.

7. Conclusions

The optimization scheme presented here shows the dependence of alkaline cell discharge behavior on initial cathode porosity and other associated internal geometry changes. Graphite removal is much more influential in improving cell performance than the variable electrode length algorithm alone. The cathode effective matrix conductivity analysis reveals that a lower σ_c value may also benefit the cell operation. Low depth of discharge predictions by the model, even for the best cases, signal that active material removal might be helpful in seeking a best design. Such a study would be worthwhile if a longer cell life and a less massive battery are successfully combined. As this study addresses only a single test condition with one galvanostatic discharge rate and cutoff voltage pairing, it is easy to visualize applying such an analysis to other industrially relevant conditions.

8. List of symbols

a_c^0	initial specific interfacial area in the cathode (cm^{-1})
c_i	concentration of species i ($\mathrm{mol/cm^3}$)
D_i	diffusion coefficient of aqueous salt i ($\mathrm{cm^2/s}$)
E	cell voltage (V)
E_0	open circuit potential after 50% discharge (V)
f	depth of discharge
f_d	depth of discharge at the cell cutoff voltage
F	Faraday's constant (96,487 C/mol)
$\boldsymbol{I}$	cell current density vector ($\mathrm{A/cm^2}$)
I	cell current (A)
i_0	cathode exchange current density at a reference condition ($\mathrm{A/cm^2}$)
$\boldsymbol{i}_2$	superficial current density in the solution phase ($\mathrm{A/cm^2}$)
L	cell height (cm)
n	number of electrons transferred in the reference electrode reaction
$\boldsymbol{N}_i$	molar flux of species i, denoting either zincate or hydroxyl ion ($\mathrm{mol/cm^2\ s}$)
Q	theoretical capacity of MnO_2 in the cathode ($\mathrm{Ah/g\text{-}MnO_2}$)
r	radial distance (cm)
r_i	current collector location i, or electrode/separator interface location i (cm)
R_i	volumetric production rate of species i, denoting either zincate or hydroxyl ion ($\mathrm{mol/cm^3\ s}$)
R	universal gas constant (8.3143 J/mol K)
s_i	stoichiometric coefficient of species i in the reference electrode reaction
t	time (s)
t_d	discharge time to reach the cutoff voltage (h)
t_i	transference number of species i with respect to the volume average velocity

T	cell temperature (K)
V_i	volume of component i, or volume of region i (cm^3)
$\boldsymbol{v}$	volume average velocity in the electrolyte (cm/s)
w_{act}	initial amount of MnO_2 in the cathode available for electrochemical reaction (g)
w_G	amount of graphite added to the MnO_2 matrix in the cathode (g)
z_i	charge number of species i

Greek

α_a	anodic transfer coefficient for the cathode electrochemical reaction
α_c	cathodic transfer coefficient for the cathode electrochemical reaction
γ	ratio of matrix to electrolyte effective electrical conductivities in the cathode
δ	dimensionless cell current using cathode parameters
ϵ	porosity
ϵ_i	porosity of region i, or solid volume fraction of species i
η	local overpotential (V)
κ	electrolyte conductivity (Ω^{-1} cm^{-1})
μ_i	electrochemical potential of aqueous salt i (J/mol)
ν	square root of the dimensionless exchange current density in the cathode
ν_{ij}	number of ions of species i contained in one molecule of salt j
ρ_G	density of graphite in the cathode (g/cm^3)
σ	effective matrix conductivity (Ω^{-1} cm^{-1})
σ_i	effective matrix conductivity of electrode region i, or electrical conductivity of solid species i (Ω^{-1} cm^{-1})
χ	fraction of graphite removed
ω_G	weight fraction of graphite in the total solid cathode material prior to graphite removal

Main Subscripts

A	potassium zincate
B	potassium hydroxide
0	solvent (water)
1	zincate ion
2	hydroxyl ion

Superscripts

0	initial condition

References

[1] E.J. Podlaha, H.Y. Cheh, J. Electrochem. Soc. 141 (1994) 15.
[2] E.J. Podlaha, H.Y. Cheh, J. Electrochem. Soc. 141 (1994) 28.
[3] T.I. Evans, R.E. White, J. Electrochem. Soc. 136 (1989) 2798.
[4] D. Fan, R.E. White, J. Electrochem. Soc. 138 (1991) 17.
[5] P. De Vidts, R.E. White, J. Electrochem. Soc. 142 (1995) 1509.
[6] T.F. Fuller, M. Doyle, J. Newman, J. Electrochem. Soc. 141 (1994) 1.
[7] M. Doyle, J. Newman, A.S. Gozdz, C.N. Schmutz, J.-M. Tarascon, J. Electrochem. Soc. 143 (1996) 1890.
[8] B. Paxton, J. Newman, J. Electrochem. Soc. 144 (1997) 3818.
[9] G.S. Nagarajan, J.W. Van Zee, R.M. Spotnitz, J. Electrochem. Soc. 145 (1998) 771.
[10] J. Newman, J. Electrochem. Soc. 142 (1995) 97.
[11] A. Kozawa, R.A. Powers, Electrochem. Technol. 5 (1967) 535.
[12] J. Newman, W. Tiedemann, AIChE J. 21 (1975) 25.
[13] Z. Mao, R.E. White, J. Electrochem. Soc. 139 (1992) 1105.
[14] W.G. Sunu, PhD thesis, University of California, Los Angeles, CA, 1978.
[15] E.J. Podlaha, PhD thesis, Columbia University, New York, 1992.
[16] W.C. Maskell, J.E.A. Shaw, F.L. Tye, J. Power Sources 8 (1982) 113.
[17] Duracell Alkaline–Manganese Dioxide Technical Bulletin, available at http://www.duracell.com/OEM/index.html (select 'Alkaline Manganese Dioxide' link after choosing 'Primary Systems' link).
[18] R.H. Perry, D.W. Green, J.O. Maloney (Eds.), Chemical Engineers' Handbook, 6th edn., McGraw-Hill, New York, 1984, p. 3-11.
[19] J. Newman, Electrochemical Systems, 2nd edn., Prentice-Hall, Englewood Cliffs, NJ, 1991, pp. 539–555.
[20] J. Van Zee, G. Kleine, R.E. White, J. Newman, in: R.E. White (Ed.), Electrochemical Cell Design, Plenum, New York, 1984, pp. 377–389.
[21] D.N. Bennion, AIChE Symp. Ser. 79 (1983) 25.
[22] C.Y. Mak, H.Y. Cheh, G.S. Kelsey, P. Chalilpoyil, J. Electrochem. Soc. 138 (1991) 1607.
[23] T.I. Evans, T.V. Nguyen, R.E. White, J. Electrochem. Soc. 136 (1989) 328.
[24] J.S. Chen, H.Y. Cheh, J. Electrochem. Soc. 140 (1993) 1205.
[25] P. Ruetschi, J. Electrochem. Soc. 131 (1984) 2737.
[26] B.D. Desai, J.B. Fernandes, V.N. Kamat Dalal, J. Power Sources 16 (1985) 1.
[27] W.C. Vosburgh, J. Electrochem. Soc. 106 (1959) 839.
[28] W.J. Wruck, PhD thesis, University of Wisconsin, Madison, WI, 1984.
[29] M. Doyle, T.F. Fuller, J. Newman, J. Electrochem. Soc. 140 (1993) 1526.